LETTERS
PUBLISHED ONLINE: 3 MARCH 2013 | DOI: 10.1038/NMAT3575
nature materials

Artificially engineered superlattices of pnictide superconductors

S. Lee[1], C. Tarantini[2], P. Gao[3], J. Jiang[2], J. D. Weiss[2], F. Kametani[2], C. M. Folkman[1], Y. Zhang[3], X. Q. Pan[3], E. E. Hellstrom[2], D. C. Larbalestier[2] and C. B. Eom[1]*

Significant progress has been achieved in fabricating high-quality bulk and thin-film iron-based superconductors. In particular, artificial layered pnictide superlattices[1,2] offer the possibility of tailoring the superconducting properties and understanding the mechanism of the superconductivity itself. For high-field applications, large critical current densities (J_c) and irreversibility fields (H_{irr}) are indispensable along all crystal directions. On the other hand, the development of superconducting devices such as tunnel junctions requires multilayered heterostructures. Here we show that artificially engineered undoped Ba-122/Co-doped Ba-122 compositionally modulated superlattices produce *ab*-aligned nanoparticle arrays. These layer and self-assemble along *c*-axis-aligned defects[3–5], and combine to produce very large J_c and H_{irr} enhancements over a wide angular range. We also demonstrate a structurally modulated $SrTiO_3$(STO)/Co-doped Ba-122 superlattice with sharp interfaces. Success in superlattice fabrication involving pnictides will aid the progress of heterostructured systems exhibiting new interfacial phenomena and device applications.

Since the discovery of iron-based superconductors[6–11], epitaxial thin films have been successfully grown by many groups[3,12–18], thus significantly advancing their potential for device applications and the understanding of their fundamental physical properties[12,19–25]. In particular, we reported high-quality Co-doped $BaFe_2As_2$(Ba-122) single-crystal thin films using template engineering that generated *c*-axis-aligned, self-assembled, second-phase nanorods[3–5] as schematized in Fig. 1a. These nanorods yielded strong *c*-axis pinning centres that enhance the in-field critical current density, J_c. The *c*-axis pinning was so strong that it was able to invert the usual irreversibility field anisotropy in which H_{irr} parallel to the *ab* plane is 1.5–2 times that parallel to the *c* axis. This motivated us to consider using multilayer growth methods to enhance the *ab*-plane properties because high-field applications prefer to enhance J_c in all field configurations, as sketched in Fig. 1c. We note that no study of artificially controlled flux pinning for pnictide superconductors has yet been reported, whereas many investigations of J_c and irreversibility field (H_{irr}) enhancement by nanoparticle incorporation have been performed in the high-T_c cuprate superconductor $YBa_2Cu_3O_{7-x}$ (YBCO) such as that using YBCO/Y_2BaCuO_5 and YBCO/$BaZrO_3$ multilayers[26,27]. However, every material system is different and it is striking that pinning engineering has not yet been demonstrated in either the Bi-2212 or Bi-2223 systems or even the most classical high-field superconductor, Nb_3Sn, even though it is very possible and valuable in YBCO. This motivation underpinned our studies of this Fe-based superconductor system. A major difference between YBCO- and Fe-based superconductor systems is that Fe-based superconductors are metallic and it thus seemed questionable whether insulating epitaxial oxide pinning centres grown parallel to the *ab* planes could be incorporated without suppressing the superconductivity of the Ba-122 matrix. We were at first doubtful that multiple epitaxial layers of a Ba-122 metal phase and an oxide phase could be grown with high crystalline perfection because they might have been structurally and chemically incompatible but in fact we here demonstrate that structurally and compositionally modulated superlattices of oxide can be grown in the matrix of a Ba-122 metallic system, a result that is significantly different from the YBCO oxide superconductor system, where both the oxide matrix and the pinning phase are structurally and chemically compatible. We see that this enables strong vortex pinning and opens up the possibility of growing superconducting superlattice structures (schematized in Fig. 1b) that can be used as a means for understanding fundamental mechanisms of superconductivity and development of superconducting devices such as pnictide tunnel junctions.

Taking account of the metallic properties of Ba-122, which does not contain oxygen and is easily compromised by impurities, we narrowed down the possible interlayer to two different types of model superlattice structure. As we previously found[3] that a divalent, alkaline earth element-containing oxide such as $SrTiO_3$ (STO) is an excellent platform on which to grow Co-doped Ba-122 thin films owing to their common features, STO was our first choice. This led to a structurally modulated superlattice with sharp interfaces, devoid of *c*-axis defects. The second choice of interlayer was undoped Ba-122 made from an oxygen-rich, Co-free 122 target (O–Ba-122) where the interlayer has a similar structure but slightly different lattice parameters. This led to compositionally modulated O–Ba-122/Co-doped Ba-122 superlattice. Our hypothesis was that oxygen-rich undoped Ba-122 would facilitate the formation of strong pinning, oxygen-rich precipitates along the *ab* planes, just as it had for the *c*-axis pins in single-layer films of Co-doped Ba-122.

With this approach, we have successfully grown epitaxial superlattices of $STO_{1.2\,nm}$/8% Co-doped $Ba\text{-}122_{13\,nm}$ and O–$Ba\text{-}122_{3\,nm}$/8% Co-doped $Ba\text{-}122_{13\ and\ 20\,nm}$ on 40 nm STO templates deposited on (001) (La, Sr)(Al, Ta)O_3 (LSAT) single-crystal substrates by using pulsed laser deposition. We varied the thickness of the bilayer (modulation wavelength, Λ) and the total number of bilayers (n). Their structural and superconducting properties are listed in Supplementary Table SI. To focus on the key points, we discuss here only ($STO_{1.2\,nm}$/Co-doped $Ba122_{13\,nm}$) × ($n = 24$) superlattice (hereafter referred to as STO SL) and (O–$Ba\text{-}122_{3\,nm}$/Co-doped $Ba122_{13\,nm}$) × ($n = 24$) superlattice (hereafter referred to as O–Ba-122 SL).

[1]Department of Materials Science and Engineering, University of Wisconsin-Madison, Madison, Wisconsin 53706, USA, [2]Applied Superconductivity Center, National High Magnetic Field Laboratory, Florida State University, 2031 East Paul Dirac Drive, Tallahassee, Florida 32310, USA, [3]Department of Materials Science and Engineering, The University of Michigan, Ann Arbor, Michigan 48109, USA. *e-mail: eom@engr.wisc.edu.

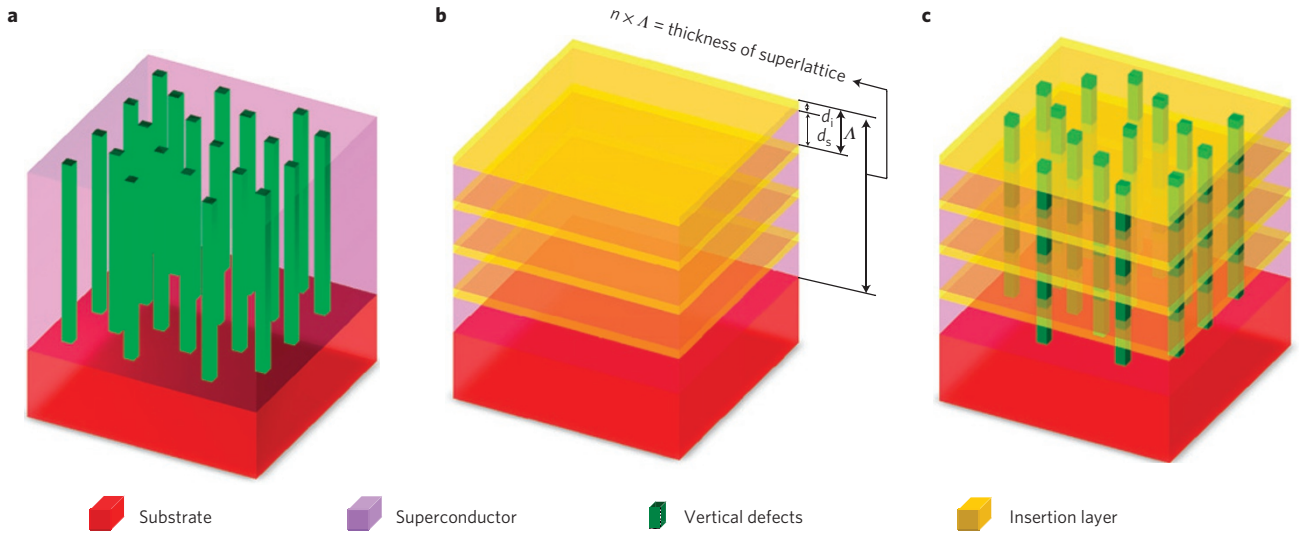

Figure 1 | Schematic representations of various structures of superconductor epitaxial thin films. a, Superconductor thin film with defects along the *c* axis. **b**, Superlattice structure (d_i, thickness of an insertion layer; d_s, thickness of a superconductor layer; Λ (modulation wavelength) $= d_i + d_s$; *n*, total number of bilayers). **c**, Superlattice structure with defects along the *c* axis.

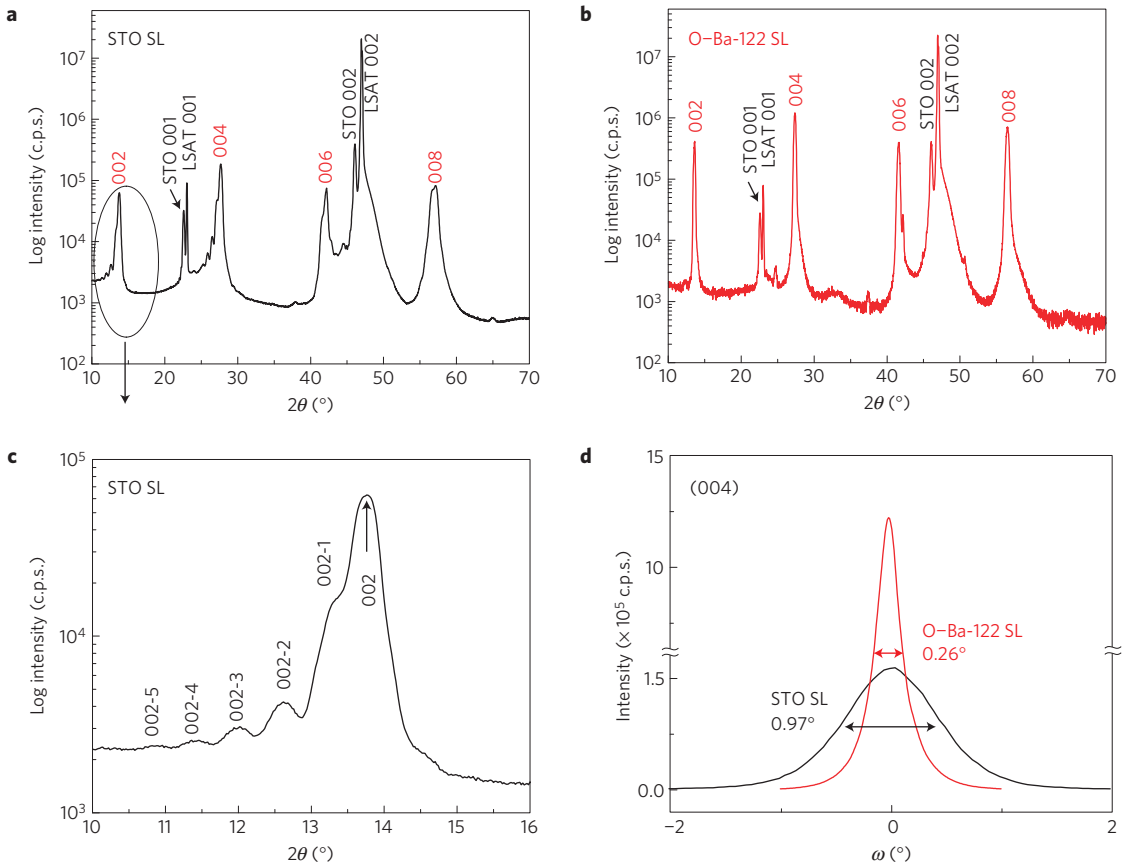

Figure 2 | XRD patterns obtained on O–Ba-122-inserted and STO-inserted Co-doped $BaFe_2As_2$ superlattices. a, Out-of-plane θ–2θ XRD pattern of $(STO_{1.2\,nm}/\text{Co-doped Ba-122}_{13\,nm}) \times 24$. **b**, Out-of-plane θ–2θ XRD pattern of $(\text{O–Ba-122}_{3\,nm}/\text{Co-doped Ba-122}_{13\,nm}) \times 24$. **c**, Magnification of the area outlined in **a** near the 002 reflection of $(STO_{1.2\,nm}/\text{Co-doped Ba-122}_{13\,nm}) \times 24$. **d**, Rocking curves and FWHM for the (004) reflection of two superlattices.

The epitaxial crystalline quality and modulation wavelength (Λ) of the superlattices were determined by four-circle X-ray diffraction (XRD) with a Cu Kα source ($\lambda = 1.5405$ Å). Figure 2a shows the θ–2θ scan of the STO SL. The XRD pattern shows that Co-doped Ba-122 00*l* reflections dominate, which indicates *c*-axis epitaxial growth normal to the STO template and LSAT substrate. Figure 2c shows a magnification of Fig. 2a close to the 002 reflection of the STO SL that clearly shows satellite peaks with calculated modulation length $\Lambda = 14\,\text{nm} \pm 2\,\text{nm}$ the same as the nominal Λ. Rocking curves for the 004 reflection were measured to determine the out-of-plane mosaic spread and crystalline quality. As shown in Fig. 2d, the full-width at half-maximum (FWHM) of the 004

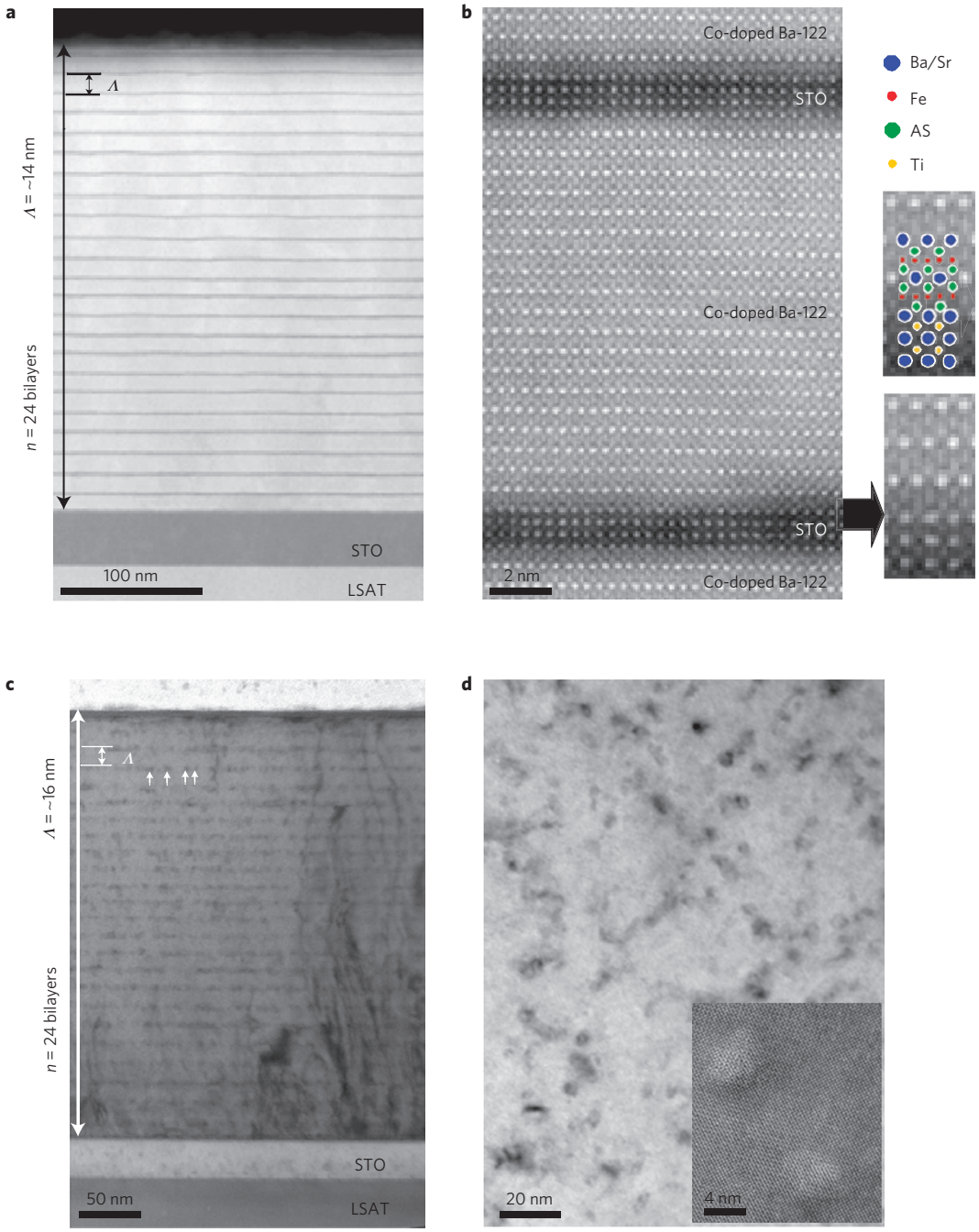

Figure 3 | Microstructure of Co-doped $BaFe_2As_2$ superlattice thin films investigated by TEM. a,**b**, High-angle annular dark-field image of the ⟨100⟩ projection of $(STO_{1.2\,nm}/Co\text{-doped Ba-122}_{13\,nm}) \times 24$. **c**, Cross-sectional TEM image of the ⟨100⟩ projection of $(O\text{-Ba-122}_{3\,nm}/Co\text{-doped Ba-122}_{13\,nm}) \times 24$. Arrows indicate nanoparticle arrays in the O-Ba-122 layer along the *ab* axis. **d**, Planar-view TEM image of $(O\text{-Ba-122}_{3\,nm}/Co\text{-doped Ba-122}_{13\,nm}) \times 24$ showing vertical defects along the *c* axis. Inset: high-resolution image of the vertical defects.

reflection rocking curve of STO SL is 0.97°. Furthermore, the STO SL exhibits strong and sharp peaks ($\Delta\phi = 1.1°$) only every 90° in the azimuthal phi scan of the off-axis 112 reflection of Co-doped Ba-122 (Supplementary Fig. S1a), revealing a good in-plane epitaxy. These results confirm the excellent epitaxial arrangement, even though as many as 24 STO/Co-doped Ba-122 bilayers were grown.

Figure 2b shows the θ–2θ scan of the O–Ba-122 SL and it shows excellent *c*-axis epitaxial growth. Figure 2d shows the FWHM of the 004 reflection rocking curve of the O–Ba-122 SL to be as narrow as 0.26°, which is far superior to the STO SL and even better than other reports about single-layer Ba-122 thin films[13,16]. Furthermore, as shown in Supplementary Fig. S1, the azimuthal phi scan of the O–Ba-122 SL shows much sharper peaks ($\Delta\phi = 0.69°$) than the STO SL. The reason why O–Ba-122 SL has superior crystalline quality is that O–Ba-122 and Co-doped Ba-122 are structurally identical, differing only by the 8% cobalt addition. As the atomic scattering factors of Co and Fe are very close it would be exceedingly difficult to see any satellite peaks by XRD.

To investigate the microstructure of STO and O–Ba-122 SLs, transmission electron microscopy (TEM) was used. Figure 3a,b shows cross-sectional low- and high-magnification high-angle annular dark-field images of the STO SL. In Fig. 3a, the bright and dark layers correspond to 13 nm Co-doped Ba-122 and 1.2 nm STO layers, respectively. We can clearly see that there are 24

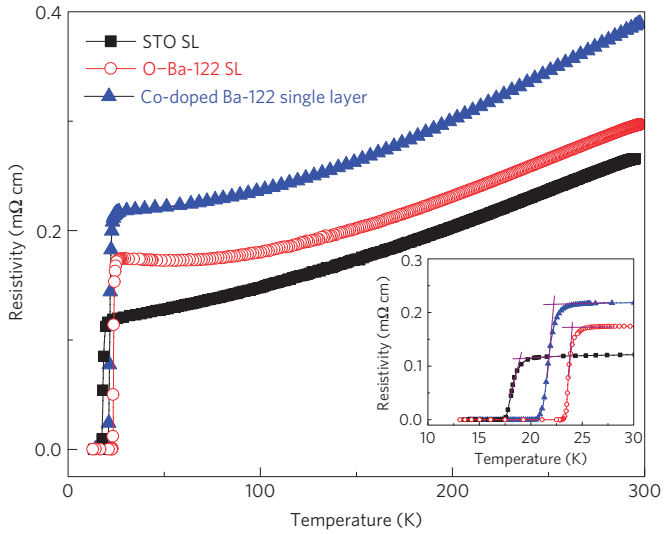

Figure 4 | Resistivity as a function of temperature. $\rho(T)$ from room temperature to below T_c. Inset: superconducting transition of all films.

STO/Co-doped Ba-122 bilayers and Λ is 14 nm in accordance with our design and the modulation wavelength determined by XRD. Furthermore, 3-unit-cell-thick STO interlayers have been uniformly grown on the Co-doped Ba-122 layer as shown in Fig. 3b. This indicates that we can control the thickness of the STO interlayer with single-unit-cell precision and maintain a sharp interface between STO and Co-doped Ba-122. A schematic representation of the ⟨100⟩ projection of Co-doped Ba-122 and STO at the interface is shown to the right of Fig. 3b, where the bonding of the FeAs layer to the SrO layer in STO is quite evident, in excellent agreement with the hypothesis we previously proposed[3].

Figure 3c is a cross-sectional TEM image of the O–Ba-122 SL, which clearly shows 24 bilayers and the modulation wavelength $\Lambda = 16$ nm. The planar-view TEM image (Fig. 3d) exhibits c-axis -aligned defects as we observed in the single-layer Co-doped Ba-122 in our previous reports[4,5]. The first interesting point is that the interface O–Ba-122 layers have grown as laterally aligned but discontinuous second-phase nanoparticles of several nanometres in size. Presumably, island growth of the oxygen-containing second phase is energetically favourable owing to the small lattice mismatch with the Co-doped Ba-122 SL. Similar discontinuous growth was observed with $YBa_2Cu_3O_7/YBa_2CuO_5$ multilayers[26]. The second interesting point is that the O–Ba-122 SL has c-axis defects extending across many ab-axis-aligned nanoparticle arrays, whereas the STO SL does not have such c-axis-aligned defects. We infer that oxygen, which is needed to produce the c-axis-aligned defects, is absorbed by the STO interlayers under our high-vacuum, high-temperature growth conditions. The structure of the O–Ba-122 SL is thus akin to Fig. 1c, which is more desirable than the structure of the STO SL (Fig. 1b) for flux pinning, because the O–Ba-122 SL has structural defects in both the c- and ab-axis directions. Strictly speaking, the actual morphology of the O–Ba-122 SL is close to Fig. 1c with nanoparticles rather than a continuous bilayer interface.

To characterize the superconducting transition temperature T_c, resistivity was measured as a function of temperature (ρ–T) by the van der Pauw method. As shown in Fig. 4 the residual resistivity ratio of the O–Ba-122 SL (1.7) is slightly lower than that of the STO SL (2.2). In the inset of Fig. 4, the O–Ba-122 SL shows high $T_{c,\rho=0} = 22.9$ K, and narrow ΔT_c of 1.1 K, which indicates the good quality of these layered films even in the presence of a significant lateral second phase. In contrast, $T_{c,\rho=0}$ of the ultrathin layers of the STO SL is suppressed to 17.0 K. Evidently, compatibility between the O–Ba-122 and Co-doped Ba-122 is better than that between STO and Co-doped Ba-122. Figure 4 also indicates a $T_{c,\rho=0}$ of 20.5 K for ∼400-nm-thick single-layer Co-doped Ba-122 film[5] deposited on 40 nm STO/LSAT.

To understand the effect of this nanostructural engineering on J_c and H_{irr} we made extensive characterizations at various temperatures, fields and field orientations to the crystal axes. Figure 5a shows $J_c(H)$ for $H \| c$ at 4.2 K far from T_c. It is immediately clear that the two samples with c-axis nanorod pinning defects have much higher $J_c(H)$ and $H_{irr}(T)$. The influence of the ab-plane defects is revealed in Fig. 5b, where the J_c anisotropy for the O–Ba-122 SL and Co-doped Ba-122 single layers at 16 K for perpendicular ($H \| c$) and parallel ($H \| ab$) configurations is compared. Despite these data being affected by their T_c differences (the O–Ba-122 SL has a higher T_c, consistent with its higher J_c), both samples have the same $H_{irr} \sim 11$ T for H parallel to the c axis, a result consistent with the lower density of c-axis pinning centres in O–Ba-122 SL compared with the single-layer Co-doped Ba-122. However, the most striking result is that the inverted H_{irr} anisotropy seen for the single-layer film with only c-axis defects (H_{irr} for $H \| ab$ is less than for $H \| c$) is corrected when ab-plane pins are present in the O–Ba-122 SL film. It is clear that H_{irr} for $H \| ab$ ($H_{irr,ab}$) of O–Ba-122 SL is approximately doubled from 9 to ∼ 19 T, restoring the expected anisotropy of H_{irr} and $J_c(H)$ without any degradation to the c-axis properties. This enhancement is due to the presence of the ab-plane-aligned nanoparticles in the O–Ba-122 SL shown in Fig. 3.

The angular transport J_c of the STO SL, O–Ba-122 SL and Co-doped Ba-122 single layer[3–5] shown in Fig. 5c evaluated at a constant reduced temperature $T/T_c \sim 0.6$ provides further insight into the pinning effects of the nanoparticles. The Co-doped Ba-122 single layer[3–5] shows only the strong c-axis pinning produced by the

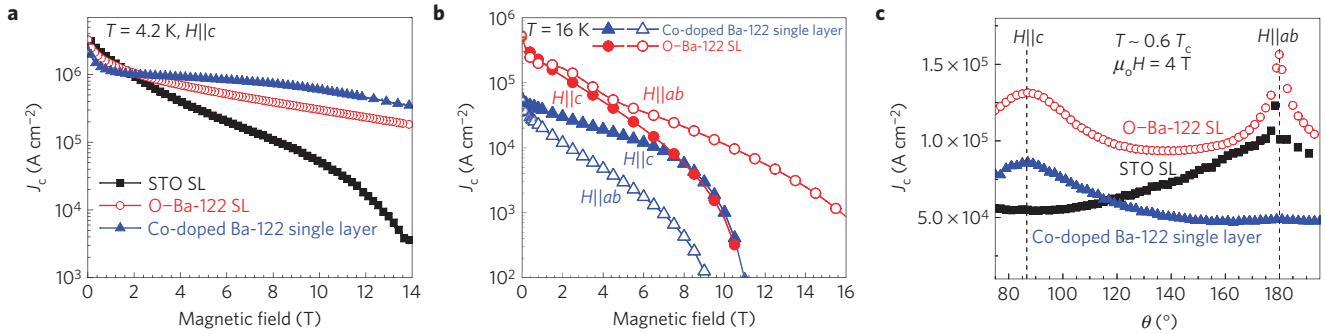

Figure 5 | Critical current density as a function of magnetic field. a, Magnetization J_c as a function of magnetic field at 4.2 K with the field applied perpendicular to the plane of all three films. **b**, Transport J_c as a function of magnetic field at 16 K with the field applied perpendicular and parallel to the plane of (O-Ba-$122_{3\,nm}$/Co-doped Ba-$122_{13\,nm}$) × 24 and Co-doped Ba-122 single-layer thin films. **c**, Angular dependence of transport J_c at 4 T for all three films at a reduced temperature of $T/T_c = \sim 0.6$.

correlated, self-assembled nanopillars, whereas the J_c of the STO SL shows only a sharp, few-degrees-wide peak when the magnetic field is aligned with the *ab*-plane STO superlattice. The $J_c(\theta)$ of O–Ba-122 SL is higher than the other two samples and shows both strong *ab*-plane and *c*-axis peaks, which is quite consistent with the *ab*-plane-aligned second-phase nanoparticles of the bilayer and its *c*-axis-aligned defects, seen in Fig. 3c,d. Very strong pinning in fields up to 45 T has been reported elsewhere[28].

We have grown artificially layered superlattice structures in Co-doped Ba-122 thin films with controlled structural and compositional modulations. The insertion of O–Ba-122 layers allows nanoparticle formation that introduces strong vortex pinning along the *ab*-planes while still allowing the formation of vertically aligned defects. The remarkable enhancement of the pinning properties over a wide angular range related to the *ab*-plane nanoparticles is highlighted by the significant increase of the irreversibility field and by much improved J_c. The engineered structures presented here are surely capable of further refinement by optimizing interlayer separation and the composition of the vortex pinning layers, features that cannot be obtained in single-layer films. The successful growth of such high-quality artificially layered structures will have wide implications for achieving new interface-driven high-T_c superconductivity[29] and potential device applications involving superconductor–normal–superconductor and superconductor–insulator–superconductor junctions[30]. Furthermore, artificially fabricated multilayer structures can also be used as model systems to study many physical phenomena such as dimensionality, the proximity effect and interface pinning.

Methods

(1.2 nm STO or 3 nm O–Ba-122/13 nm and 20 nm Co-doped Ba-122) × *n* superlattice thin films were grown *in situ* on STO-templated (001)-oriented LSAT single-crystal substrates using pulsed laser deposition with a KrF (248 nm) ultraviolet excimer laser in a vacuum of 3×10^{-4} Pa at 730–750 °C. The base pressure before deposition was 3×10^{-5} Pa, and the deposition took place at 3×10^{-4} Pa owing to degassing of the substrate heater. Laser triggering, ablation time and target rotation were automatically controlled by a computer program during the superlattice deposition. It took 5 s to change the target position and laser triggering between the Co-doped Ba-122 and O–Ba-122. The magnetization of films that were about 2 mm × 4 mm was measured in a 14 T Oxford vibrating sample magnetometer at 4.2 K with the applied field perpendicular to the film surface. For a thin film, $J_c = 15\Delta m/(Vr)$, where Δm is the width of the hysteresis loop in electromagnetic units, V is the film volume in cubic centimetres and r is the radius corresponding to the total area of the sample size, and was calculated from $\pi r^2 = a \times b$ (a and b are the film width and length in centimetres, respectively).

Received 3 April 2012; accepted 25 January 2013; published online 3 March 2013

References

1. Triscone, J-M. *et al.* $YBa_2Cu_3O_7/PrBa_2Cu_3O_7$ superlattices—properties of ultrathin superconducting layers separated by insulating layers. *Phys. Rev. Lett.* **64,** 804–807 (1990).
2. Suzuki, Y., Triscone, J-M., Eom, C. B., Beasley, M. & Geballe, T. H. Evidence for long localization length along *b* axis $PrBa_2Cu_3O_7$ in *a* axis $YBa_2Cu_3O_7$/*a*,*b* axis $PrBa_2Cu_3O_7$ superlattices. *Phys. Rev. Lett.* **73,** 328–331 (1994).
3. Lee, S. *et al.* Template engineering of Co-doped $BaFe_2As_2$ single-crystal thin films. *Nature Mater.* **9,** 397–402 (2010).
4. Zhang, Y. *et al.* Self-assembled oxide nanopillars in epitaxial $BaFe_2As_2$ thin films for vortex pinning. *Appl. Phys. Lett.* **98,** 042509 (2011).
5. Tarantini, C. *et al.* Strong vortex pinning in Co-doped $BaFe_2As_2$ single crystal thin films. *Appl. Phys. Lett.* **96,** 142510 (2010).
6. Kamihara, Y., Watanabe, T., Hirano, M. & Hosono, H. Iron-based layered superconductor $La[O_{1-x}F_x]FeAs$ ($x = 0.05$–0.12) with $T_C = 26$ K. *J. Am. Chem. Soc.* **130,** 3296–3297 (2008).
7. Chen, X. *et al.* Superconductivity at 43 K in $SmFeAsO_{1-x}F_x$. *Nature* **453,** 761–762 (2008).
8. Wang, C. *et al.* Thorium-doping-induced superconductivity up to 56 K in $Gd_{1-x}Th_xFeAsO$. *Europhys. Lett.* **83,** 67006 (2008).
9. Rotter, M., Tegel, M. & Johrendt, D. Superconductivity at 38 K in the iron arsenide $(Ba_{1-x}K_x)Fe_2As_2$. *Phys. Rev. Lett.* **101,** 107006 (2008).
10. Sefat, A. S. *et al.* Superconductivity at 22 K in co-doped $BaFe_2As_2$ crystals. *Phys. Rev. Lett.* **101,** 117004 (2008).
11. Hsu, F. C. *et al.* Superconductivity in the PbO-type structure α-FeSe. *Proc. Natl Acad. Sci. USA* **105,** 14262–14264 (2008).
12. Lee, S. *et al.* Weak-link behavior of grain boundaries in superconducting $BaFe_2As_2$ bicrystals. *Appl. Phys. Lett.* **95,** 212505 (2009).
13. Katase, T., Hiramatsu, H., Kamiya, T. & Hosono, H. High critical current density 4 MA cm^{-2} in co-doped $BaFe_2As_2$ epitaxial films grown on $(La,Sr)(Al,Ta)O_3$ substrates without buffer layers. *Appl. Phys. Express* **3,** 063101 (2010).
14. Haindl, S. *et al.* High upper critical fields and evidence of weak-link behavior in superconducting $LaFeAsO_{1-x}F_x$ thin films. *Phys. Rev. Lett.* **104,** 077001 (2010).
15. Kawaguchi, T. *et al. In situ* growth of superconducting NdFeAs(O,F) thin films by molecular beam epitaxy. *Appl. Phys. Lett.* **97,** 042509 (2010).
16. Iida, K. *et al.* Influence of Fe buffer thickness on the crystalline quality and the transport properties of $Fe/Ba(Fe_{1-x}Co_x)_2As_2$ bilayers. *Appl. Phys. Lett.* **97,** 172507 (2010).
17. Katase, T. *et al.* Advantageous grain boundaries in iron pnictide superconductors. *Nature Commun.* **2,** 409 (2011).
18. Iida, K. *et al.* Epitaxial growth of superconducting $Ba(Fe_{1-x}Co_x)_2As_2$ thin films on technical ion beam assisted deposition MgO substrates. *Appl. Phys. Express* **4,** 013103 (2011).
19. Baily, S. *et al.* Pseudoisotropic upper critical field in cobalt-doped $SrFe_2As_2$ epitaxial films. *Phys. Rev. Lett.* **102,** 117004 (2009).
20. Katase, T. *et al.* Josephson junction in cobalt-doped $BaFe_2As_2$ epitaxial thin films on $(La,Sr)(Al,Ta)O_3$ bicrystal substrates. *Appl. Phys. Lett.* **96,** 142507 (2010).
21. Mehta, M. *et al.* Conductance asymmetry in point-contacts on epitaxial thin films of $Ba(Fe_{0.92}Co_{0.08})_2As_2$. *Appl. Phys. Lett.* **97,** 012503 (2010).
22. Perucchi, A. *et al.* Multi-gap superconductivity in a $BaFe_{1.84}Co_{0.16}As_2$ film from optical measurements at terahertz frequencies. *Euro. Phys. J. B* **77,** 25–30 (2010).
23. Sheet, G. *et al.* Phase-incoherent superconducting pairs in the normal state of $Ba(Fe_{1-x}Co_x)_2As_2$. *Phys. Rev. Lett.* **105,** 167003 (2010).
24. Aguilar, R. V. *et al.* Pair-breaking effects and coherence peak in the terahertz conductivity of superconducting $BaFe_{2-2x}Co_{2x}As_2$ thin films. *Phys. Rev. B* **82,** 180514 (2010).
25. Yong, J. *et al.* Superfluid density measurements of $Ba(Co_xFe_{1-x})_2As_2$ films near optimal doping. *Phys. Rev. B* **83,** 104510 (2011).
26. Haugan, T., Barnes, P. N., Wheeler, R., Meisenkothen, F. & Sumption, M. Addition of nanoparticle dispersions to enhance flux pinning of the $YBa_2Cu_3O_{7-x}$ superconductor. *Nature* **430,** 867–870 (2004).
27. Kiessling, A. *et al.* Nanocolumns in $YBa_2Cu_3O_{7-x}/BaZrO_3$ quasi-multilayers: Formation and influence on superconducting properties. *Supercond. Sci. Technol.* **24,** 055018 (2011).
28. Tarantini, C. *et al.* Artificial and self-assembled vortex-pinning centers in superconducting $Ba(Fe_{1-x}Co_x)_2As_2$ thin films as a route to obtaining very high critical-current densities. *Phys. Rev. B* **86,** 214504 (2012).
29. Gozar, A. *et al.* High-temperature interface superconductivity between metallic and insulating copper oxides. *Nature* **455,** 782–785 (2008).
30. Covington, M. *et al.* Observation of surface-induced broken time-reversal symmetry in $YBa_2Cu_3O_7$ tunnel junctions. *Phys. Rev. Lett.* **79,** 277–280 (1997).

Acknowledgements

Work at the University of Wisconsin was financially supported by the DOE Office of Basic Energy Sciences under award number DE-FG02-06ER46327. The work at the NHMFL was supported under NSF Cooperative Agreement DMR-1157490 and DMR-1006584, and by the State of Florida. TEM work was carried out at the University of Michigan and was supported by the Department of Energy under grant DE-FG02-07ER46416 and the National Science Foundation DMR-0723032 (aberration-corrected TEM instrument). We would like to thank D. Fong and J. Karapetrova and the APS for synchrotron experiments. S.L and C.B.E. would like to thank S. Patnaik for helpful discussions. X.Q.P. would like to thank M. Kawasaki for the use of the aberration-corrected TEM.

Author contributions

S.L. fabricated Ba-122 superlattices, analysed epitaxial arrangement by XRD and prepared the manuscript. C.T. carried out electromagnetic characterization and prepared the manuscript. P.G., F.K. and Y.Z. carried out TEM measurements. J.D.W. fabricated Ba-122 pulsed laser deposition targets for thin-film deposition. J.J. carried out electromagnetic characterizations. C.B.E., D.C.L., E.E.H. and X.Q.P. supervised the experiments and contributed to manuscript preparation. C.B.E. conceived and directed the research. All authors discussed the results and implications and commented on the manuscript at all stages.

Additional information

Supplementary information is available in the online version of the paper. Reprints and permissions information is available online at www.nature.com/reprints. Correspondence and requests for materials should be addressed to C.B.E.

Competing financial interests

The authors declare no competing financial interests.